Microporous and Mesoporous Materials 303 (2020) 110264

Contents lists available at ScienceDirect

Microporous and Mesoporous Materials

journal homepage: http://www.elsevier.com/locate/micromeso

Tailor-engineered structural and physico-chemical properties of anodic alumina nanotubes by pulse anodization: A step forward

J.T. Domagalski [a], E. Xifre-Perez [a], A. Santos [b,c,d], J. Ferre-Borrull [a], L.F. Marsal [a,*]

[a] Departament d'Enginyeria Electrònica, Elèctrica i Automàtica, Universitat Rovira i Virgili, Avinguda dels Països Catalans, 26, 43007, Tarragona, Spain
[b] School of Chemical Engineering and Advanced Materials, The University of Adelaide, Adelaide, South Australia, 5005, Australia
[c] Institute for Photonics and Advanced Sensing, The University of Adelaide, Adelaide, South Australia, 5005, Australia
[d] ARC Centre of Excellence for Nanoscale BioPhotonics, The University of Adelaide, Adelaide, South Australia, 5005, Australia

ARTICLE INFO

Keywords:
Porous anodic alumina
Pulse anodization
Aluminum oxide nanotubes
Current density
Post-treatment

ABSTRACT

A study on advanced structural engineering of anodic alumina nanotubes (AANTs) manufactured by pulse anodization is presented. In-depth analysis of the electrochemical parameters of pulse anodization was carried out, distinctive sections of the anodization were defined. Evolution of the profiles has been quantified and described with regards to different current density applied and pulse duration during hard anodization. A smart combination of different anodization conditions enables precise control over the nanotubes' geometric features and physiochemical properties. Nanotubes are produced with varying pulse period, current density level and various post-anodization treatments (different sonication time, temperature and thermal annealing of anodic alumina film before fragmentation) under galvanostatic mode in sulfuric acid electrolyte modified with 10% (v) ethanol. The average length of nanotubes is tailor-engineered from 424 ± 92 to 1010 ± 118 nm, with an average inner diameter that ranges from 37 to 48 nm. It is also demonstrated that the level of current density input during pulse anodization has a direct effect on the ζ-potential of nanotubes, which can be tuned between 25 and 8.5 mV. Additionally, it is possible to produce nanotubes with a negative ζ-potential of −6.3 mV upon post-annealing treatment. Separation of nanotubes from the original template is improved by sonication at low temperature, providing a new means of increasing the production yield of these nanostructures. Furthermore, nanotubes are found to increasingly degrade with the bath temperature during separation. To better understand the impact of the fabrication parameters over the physical and chemical properties of nanotubes is a key step to design and tailor-engineer these model 1D nanostructures for specific applications. AANTs provide many attractive features that could find broad applicability in disciplines such as catalysis, drug delivery, nanofabrication and sensing.

1. Introduction

Anodization is an electrochemically driven process widely used in industry to passivate and modify the properties of metals (e.g. color, wear resistance, wettability) by growing a layer of insoluble anodic oxide. The metal of interest (anode) – typically aluminum alloys and other valve metals such as magnesium, zinc or titanium – is immersed into an acid electrolyte and electrochemically oxidized (anodized) under controlled conditions [1]. Application of current density (galvanostatic mode) or potential (potentiostatic mode) input signal drives the growth of anodic oxide layers in which two competing processes occur: i) current-driven growth of the metal oxide at the interface metal/oxide and ii) chemical dissolution of the oxide at the oxide/electrolyte interface [2,3]. Under appropriate anodization conditions, the aluminum oxide layer can be produced with straight cylindrical pores from top to bottom, which grow perpendicularly to the underlying metal [4,5]. The most widespread method to fabricate highly-ordered aluminum oxide for research applications is the two-step anodization, which is typically performed under potentiostatic conditions [6]. This seminal discovery boosted intensive research in this area with an exponential raise of publications on anodic alumina (AA) with mesoporous structure [7,8]. The two-step anodization process is performed under the so-called mild anodization (MA) conditions – relatively low input voltage and moderate electrolyte temperatures – which provides the highest ordering in

* Corresponding author.
E-mail addresses: jakub.domagalski@urv.cat (J.T. Domagalski), elisabet.xifre@urv.cat (E. Xifre-Perez), abel.santos@adelaide.edu.au (A. Santos), josep.ferre@urv.cat (J. Ferre-Borrull), lluis.marsal@urv.cat (L.F. Marsal).

https://doi.org/10.1016/j.micromeso.2020.110264
Received 27 January 2020; Received in revised form 15 April 2020; Accepted 16 April 2020
Available online 24 April 2020

mesoporous structure after initial stabilization of pore growth.

There are sets of conditions of aluminum anodization causing self-ordered growth of anodic alumina being commonly described in the literature as "standard" due to long history of application and their prevalence in the field: sulfuric acid at 25 V, oxalic acid at 40 V and phosphoric acid at 195 V. These honeycomb-like mesoporous structures are created with interpore distances of 63, 100 and 500 nm respectively [2,6,9]. But as more novel structures are discovered extend of structure geometry expands enabling aluminum anodization process to fit even better for specific application. As example, selenic acid (H_2SeO_4) AA provide promising properties with possibility to create highly ordered narrow pores of 10 nm diameter previously achievable only with sulfuric acid, which along with high transparency and lack of material photoluminescence provide for high potential of such structures [10]. Additionally, selenic acid anodization can yield self-ordering process covering interpore distance between 120 and 160 nm (at 60–100 V) which was not accessible before [11]. Another less common variant of anodization is one performed in phosphonic acid (H_3PO_3). Its recent discovery cover new range of interpore distance available with aluminum anodization – from 370 to 440 nm at voltage range between 150 and 180 V [12]. These new findings with regards to anodization regimes – even if providing only narrow window when self-arrangement occurs – cumulatively provide for better accessibility of the technique for specific application. When anodization is performed under conditions that are outside the self-ordering regimes, the spatial ordering ratio of pores in anodic alumina decreases dramatically. After initial pore nucleation, stable growth of the AA film is achieved during anodization due to dynamic equilibrium between the formation and dissolution of the oxide [13]. However, two-step anodization requires remarkably long fabrication times (>24 h). Further to that, AA's geometric features under mild anodization conditions are constrained within a limited range of dimensions (i.e. pore diameter, interpore distance). These intrinsic limitations encouraged researchers to find alternative anodization conditions that overcome these technical constraints [14–16].

While so-called hard anodization (HA) is a process known for many decades [17], for long time it was left aside in scientific research. Major constraint of HA is the amount of heat generated at the pore bottom associated with Joule effect which can lead to dramatic electric breakdown (or burning) and result in destruction of the anodic alumina film [18]. Attention to such anodization approach has been brought back with pioneering work of Lee and co-workers as they reported creation of highly ordered aluminum oxide fabricated with anodization in oxalic acid under hard anodization conditions. This allowed to create oxide films at significantly faster rates than standard anodization protocol established back then, while keeping high level of regularity [19]. Novelty of their idea relied on creation of thin layer of oxide by means of mild anodization prior to applying higher current densities, which prevented immediate electric breakdown. Hard anodization is typically performed at much higher current densities (>30 mA/cm^2) and low electrolyte temperatures. Major difference between standard anodization and HA, however, is aluminum oxide formation mechanism. During mild anodization, current density during potentiostatic anodization is determined by electric field-driven migration of ions across the oxide layer providing creation of pores prevalently at hexagonal coordination (90%). When potential increases forcing faster growth of the oxide structure, occurrence of hexagonal coordination drops up to 50% under mixed control regime. Nevertheless, further increase of the potential leads to even faster growth with depletion of specific ions at the pore bottom. As result, current density is now limited by diffusion of ionic species involved in formation of the AA, mechanism described as diffusion control characteristic for hard anodization regime. Under diffusion control process, prevalence of hexagonal arrangement reaches high values of above 80% again [20,21]. The growth rate of anodic alumina under hard anodization regime is increased ~92.5–98.7% as compared to that of mild anodization (1–3 μm/h), reaching between 40 and 80 μm h^{-1}. Hard anodization also enables the fabrication of mesoporous structures with small pore diameters, while expanding the interpore distances to longer and previously unexplored ranges, between 70 and 450 nm [14,19]. In contrast with the two-step mild anodization process, hard anodization enables fast fabrication of highly ordered mesoporous structures in one single anodization step, with processing times ~1 h [22]. 2 years later, Lee and co-workers reported modification to hard anodization that could help reduce issues related to high heat generation which was inevitable during longer HA process. New process was called pulse anodization (PA) – intercalation of pulses at high and low current density or voltage –as an optimal means to minimize the generation of heat during hard anodization and suppress electric breakdown [23]. Close observations of the AA structure produced under pulse anodization revealed nanopore diameter modulations along the oxide growth direction, which were found to precisely follow the input voltage. This finding provided a broad range of opportunities to tailor-engineer anodic alumina structures with highly sophisticated morphologies. Amongst other, diameter-modulated nanowire arrays [24], biomimetic films [25] and range of photonic crystal structures [26] such as rugate filters [27] and photonic coating for optical sensing [28] are some of AA-based nanostructures fabricated *via* pulse-like anodization process.

Efforts to optimize pulse anodization lead to higher control over the geometric features of AA structures with mesoporous modulations in depth, and to the discovery of the formation of voids along the cell boundaries during hard anodization. Pulse anodization weakens the junction strength of the nanopore cells, cracking the structure of anodic alumina along its cell boundaries. This key finding enabled pulse anodization as a new nanofabrication approach to generate 1D alumina-based nanotubes – anodic alumina nanotubes (AANTs) – with highly controlled dimensions by splitting the periodically modulated structure of anodic alumina [29,30]. Fabrication of AANTs consists of two anodization steps: i) a first step at constant mild anodization conditions to generate a starting layer of anodic alumina and ii) a pulse anodization step to modulate the nanopore diameter in depth. The starting anodic alumina layer provides mechanical integrity to the oxide film, a shuttle to achieve pore arrangement prior to pulse anodization, and prevents the film from plastic deformation and breakdown due to Joule heat generated during hard anodization. AANTs are produced by stepwise pulse anodization under current density control, in which each pulse combines a hard anodization step at high current density and a mild anodization step at low current density. The former step is responsible for the formation and engineering of AANTs, while the latter step of the pulse makes it possible to efficiently dissipate the excess of heat generated during the hard anodization step and prevent the oxide film from catastrophic burning. Another characteristic of anodization under high potential is rarely occurring phenomenon described as cell separation. Formation of such structure usually occurs during anodization with sulfuric acid at high potentials [31,32]. Usually undesired due to formation of mechanically weaker structure, properly adjusted allows for selective partition of such structure and liberation of nanoparticles [30]. So far there is no direct experimental proof pointing on the origin of these weaker spots. However, modulation of the outer walls of nanopores during pulse anodization relies strongly on the thickness of the starting anodic aluminum oxide layer. No significant outer wall modulation is observed for thicknesses of anodic alumina starting layers <65 μm. However, structural engineering of the outer nanopore walls becomes apparent at a starting layer thickness above 100 μm [33]. Such sites are mechanically more fragile than non-hydrated alumina, providing crevices to breakdown the structure of anodic alumina into nanotubes. While heat generation is usually an undesired factor in standard hard anodization [18], this phenomenon can be readily exploited to engineer weak cleavages at specific positions along the structure of anodic alumina and tailor-engineer the geometric features of nanotubes. Due to their inert chemical nature, AANTs have been devised as model nanocontainers for potential deployment in drug delivery and biomaterials applications. As-produced nanotubes with

positive surface charge (~15 mV) exhibit negative charge (−11 mV) when mixed with 10% FCS. Such nanotubes were proven to exhibit a superior non-cytotoxicity than other high aspect ratio nanomaterials, being able to load drugs within their structure and deliver efficiently their therapeutic cargoes inside cells [34,35]. The surface chemistry of nanotubes can be further modified by silanization, providing new opportunities to tune functional groups on the surface of this 1D model nanomaterial [36]. Despite advances in AANTs technology, there is still need for further fundamental and applied research in pulse anodization to achieve versatile and precise control over the structural and physiochemical properties of these unique nanostructures. Herein, we develop an advanced pulse anodization approach to tailor-engineer the structural and physiochemical properties of anodic alumina nanotubes (Fig. 1). In-depth analysis of the pulse anodization was carried out, distinctive sections of the anodization were defined. Evolution of the profiles has been quantified and described with regards to different current density applied and pulse duration during hard anodization. A smart combination of anodization conditions and post-fabrication treatments is demonstrated to provide improved control over the nanotubes' dimensions and physiochemical properties. This approach makes it possible to alter and fine-tune the structural and physico-chemical properties of nanotubes such as length, inner diameter, wall thickness, ζ-potential and crystallinity. This study lays the ground for future applications of this novel nanomaterial in disciplines such as catalysis, drug delivery, nanofabrication and sensing.

2. Experimental

2.1. Materials

Aluminum (Al) disc of thickness 0.5 mm and purity 99.999% were supplied by Goodfellow Cambridge Ltd. Sulfuric acid (H_2SO_4) and ethanol (C_2H_5OH) were purchased from Scharlau. Cooper (II) chloride ($CuCl_2$), hydrochloric acid (HCl) and perchloric acid ($HClO_4$) were purchased from Sigma-Aldrich. Chemicals were used as received, without further purification steps. PURELAB® Option-Q (18.2 MΩcm) was used for preparing all the solutions used in this study.

2.2. AANTs fabrication

Al discs 2 cm in diameter were sequentially sonicated in ethanol and ultrapure water for 10 min each. Prior to anodization, Al discs were electropolished in a mixture of $HClO_4$ and ethanol 1:4 (v/v) at 20 V and 5 °C for 7 min. Then, the first anodization step was performed in an aqueous 0.3 M H_2SO_4 electrolyte modified with 10% ethanol at 25 V and 6 °C for 20 h to generate a starting anodic alumina layer of ~100 μm.

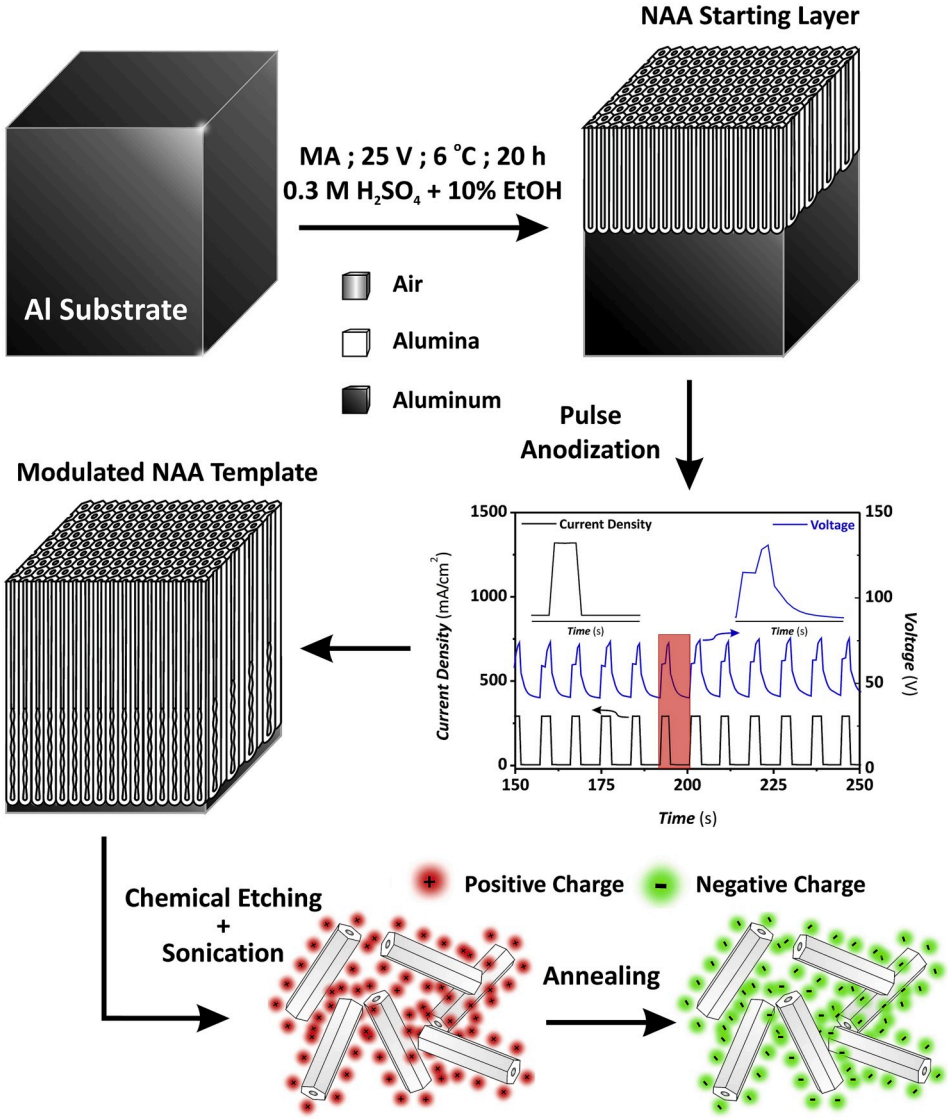

Fig. 1. Conceptual scheme describing the fabrication of AANTs by pulse anodization: MA of aluminum in sulfuric acid electrolyte followed by pulse anodization to grow an anodic alumina structure with modulated nanopore diameter (NB: representative current density–voltage profile of a modulated AA template produced with HA current density – J_{HA} = 290 mA/cm^2, MA current density – J_{MA} = 4.5 mA/cm^2, time at J_{HA} – t_{HA} = 3.5 s, and time at J_{MA} – t_{MA} = 5 s). After chemical etching and sonication nanotubes are liberated. Surface charge of AANTs can be tuned from positively to negatively charged by annealing treatment.

Next, the anodization process was switched to galvanostatic pulse anodization, using the same acid electrolyte but at 1 °C under vigorous stirring. Pulse anodization consisted of sequential pulses between mild anodization and hard anodization conditions, in which the current density (J) input was periodically switched between high and low values for a given time in a stepwise fashion. Each pulse was formed by a mild anodization step at 4.5 mA/cm^2 for 5 s and hard anodization section at 290–390 mA/cm^2 with duration between 2.0 and 3.5 s. Time analysis of individual pulse with all experimental points marked for different duration of the pulse are provided in supplementary data – Figure S1. The effective anodization area was 1.54 cm^2, and J was calculated by dividing the input current by the anodization area. After anodization, the remaining Al substrate was removed by wet chemical etching in a mixture of 0.2 M $CuCl_2$ and 6.1 M HCl followed by further immersion of the structured anodic alumina film into the same etchant solution for 1 h.

2.3. Structural and physiochemical characterization of AANTs

The geometric features and morphology of structured anodic alumina films and liberated nanotubes were analyzed by transmission electron microscopy (JEOL model 1011) and environmental scanning electron microscopy (ESEM, FEI Quanta 600). Structured films were attached to ESEM mounts with a sticky conductive carbon tape, while free-standing nanotubes were deposited by drop casting of suspension onto aluminum substrates. Structured films and nanotubes were coated with a ~5 nm thin layer of gold prior to ESEM imaging. The size distribution of nanotubes was calculated by analysis of TEM images in ImageJ, using approximately 100 individual reading points for each parameter (i.e. nanotube's length, and inner and outer nanotube diameter). ζ-Potential and size distribution profiles of anodic alumina nanotubes were analyzed by a ZetaSizer Nano, using suspension of nanotubes with a concentration of 2.5 mg/mL measured immediately after sonication. A xs analytical balance with 0.01 mg readability (KERN ABT 120-5DNM) was used during all experiments for sample weighting. Sonication was performed using a sonicating bath Bandelin Sonorex RK 102H.

2.4. Annealing and crystallographic characterization of AA and AANTs

After chemical etching and prior to liberation through sonication, structured anodic alumina films were divided into pieces and introduced into a ceramic oven (ELECTRIC LABORATORY KILN Series LKN 75) for annealing treatment at 850, 1050 and 1200 °C for 2 h. After thermal treatment, standard sonication procedure was employed. Crystallographic phases of nanotubes were analyzed by XRD measurements in a Siemens D5000 diffractometer. The source Cu_{K_α} radiation was cooper X-ray tube operated at 40 kV and 30 mA (1.54 Å). Elemental composition of AANTs produced at distinct annealing temperatures was analyzed by EDS Detector Thermo Noran Vantage that was mounted to aforementioned ESEM microscope.

3. Results

3.1. Structure of AA template and AANTs produced by pulse anodization

Fig. 2a shows a schematic description of the structure of the original anodic alumina template featuring the starting MA layer with straight nanopores and the pulsed layer (PA) with nanopore modulations in depth. A combination of selective chemical etching and sonication makes it possible to break down the structure of the AA template into AANTs. The AA structure breaks at the crevices generated at specific positions within its structure during the PA process. These crevices define the geometric features of the resulting AANTs. The geometric features defining the structure of AANTs are the nanotube length (L_{AANT}), and the nanotube inner and outer diameter (d_{in} and d_{out}). Fig. 2b–d compile a set of representative SEM images of structured anodic alumina films after this anodization process. Fig. 2b shows a top view SEM image (inset) of the AA template revealing self-organized cylindrical nanopores that follow a honeycomb-like hexagonal arrangement, with average nanopore diameter and interpore distance of 37.6 ± 2.9 nm and 64.8 ± 4.4 nm, respectively. The thicknesses of the MA and PA layers can be clearly discerned in the general cross-sectional SEM image of the AA template. The thickness of the MA layer under the conditions of study (i.e. MA at 25 V using 0.3 M H_2SO_4 electrolyte modified with 10% ethanol at 6 °C for 20 h) was 100.9 ± 1.7 μm, while the thickness of the PA layer generated by 70 MA-HA pulses at 325 and 4.5 mA/cm^2 with durations of 2.5 and 5 s was 41.3 ± 2.0 μm. The interface between the MA and PA layers can be clearly discerned by the formation of stacked layers of AA featuring nanopore modulations (Fig. 2c). Under these anodization conditions, stepwise MA-HA current density pulses can be precisely translated into modulations of nanopore diameter, which in turn generate crevices along the structure of the AA template and lead to the liberation of free-standing AANTs upon

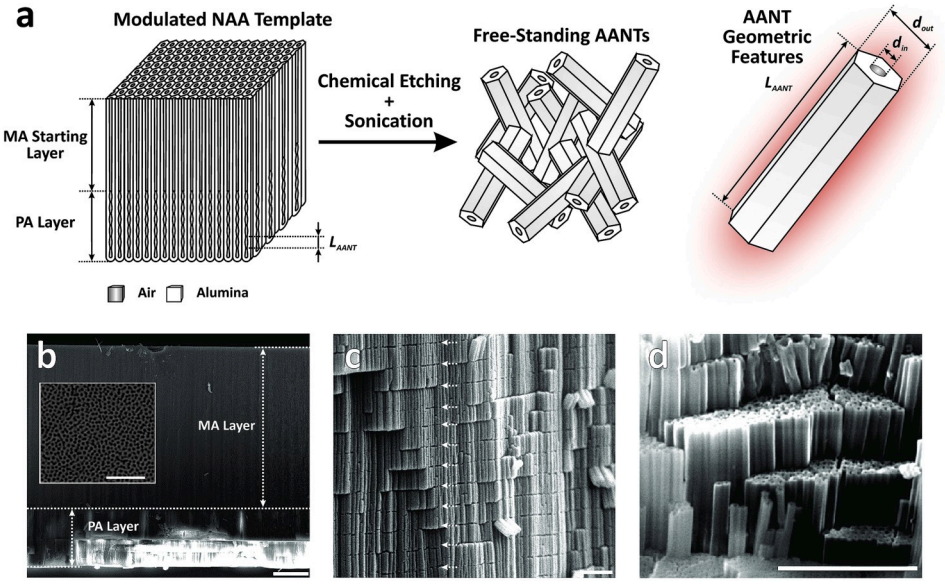

Fig. 2. Definition of geometric features and SEM characterization of modulated AA template and AANTs (NB: representative SEM images of a modulated AA template produced with HA current density – J_{HA} = 325 mA/cm^2, MA current density – J_{MA} = 4.5 mA/cm^2, time at J_{HA} – t_{HA} = 2.5 s, and time at J_{MA} – t_{MA} = 5 s). (a) Illustrated scheme of a AA template after pulse anodization (PA) and definition of geometric features of AANTs, with nanotube length (L_{AANT}), and the nanotube inner and outer diameter (d_{in} and d_{out}). (b) General cross-sectional view SEM image of a AA film with dotted line indicating the interface between the MA starting layer and the PA layer (scale bar: 20 μm) and inset showing a top view SEM image of self-organized nanopores (scale bar: 500 nm). (c) Magnified cross-sectional view SEM image showing details of nanopore modulations and structural crevices in the PA layer (scale bar: 2 μm). (d) Magnified cross-sectional view SEM image showing non-liberated AANTs within the PA layer (scale bar: 2 μm).

selective chemical etching and sonication (Fig. 2d).

3.2. Evolution of current density/voltage profile during pulse anodization

Under voltage-control mild anodization regime, nanopore growth is driven by the strength of the applied electric field and the diffusion-controlled migration of ions and electrolytic species across the oxide barrier layer. Conversely, under voltage-control hard anodization regime, nanopore growth is determined by the diffusion path of ionic species along the continuously growing nanopores. Thus, after an initial rapid increase of current density upon application of high voltage, the current density output decreases exponentially with time. This phenomenon has been attributed to the rapid growth rate and the length-dependent nature of nanopore growth under potentiostatic hard anodization conditions [14,19]. Therefore, under voltage control conditions, the growth rate of nanopores in AA produced by MA-HA pulse anodization relies on the nanopore length, making it difficult to achieve precise controllability over the nanotubes' length. However, this technical drawback can be overcome by performing MA-HA pulse anodization under current density control since under such conditions the growth rate of nanopores is constant, as established by Faraday's law [30]. Under current density-control conditions, the input current density is the main anodization parameter driving the formation of crevices along the structure of AA during the pulse anodization process. MA-HA current density pulses (input) are translated into voltage pulses (output), which are an indicator of the electrochemical phenomena occurring at the oxide barrier layer during the pulse anodization process. The shape of the output pulse anodization voltage profile can be divided into two main sections (Fig. 3a): i) an initial section of gradual increase of voltage pulse offset and amplitude (Section I); and ii) a quasi-stable state section with voltage pulse offset and amplitude (Section II) that lasts until electric breakdown occurs, which is denoted by a drastic increase of voltage amplitude. As Fig. 3b reveals, stepwise MA-HA current density pulses are translated into asymmetric sawtooth-like voltage pulses that resemble the characteristic charge–discharge cycle of an electronic capacitor. Voltage pulses can be defined by the voltage amplitude (V_{amp}) and offset (V_{offset}). Efficient formation of AANTs by PA relies strongly on the controlled generation of Joule's heat at the nanopore's bottom. Although there is no in-situ experimental method to quantify the amount of Joule's heat generated during this process, the time at which the critical temperature (T_C) is achieved at the nanopore's bottom (t_{TC}) can be established with precision by analysing the anodization profile (Fig. 3a). Formation of AANTs is denoted by the stabilization of the voltage amplitude and offset upon application of stepwise MA-HA current density pulses.

3.3. Effect of hard anodization current density on the physical and chemical properties of AANTs

The current density input is a key anodization parameter in driving the generation of AANTs by MA-HA pulse anodization. To investigate the effect of this parameter on the geometric features of AANTs, AA templates with a 100 μm thick MA starting layer were pulse-anodized with varying HA current density (J_{HA} = 290, 325 and 390 mA/cm^2). The rest of anodization parameters (i.e. MA current density – J_{MA}, time at J_{MA} – t_{MA}, and time at J_{HA} – t_{HA}) were kept constant at 4.5 mA/cm^2, 5 s and 3.5 s, respectively. Fig. 4a–c shows representative current density–voltage PA anodization profiles at varying HA current density (i.e. J_{HA} = 290, 325 and 390 mA/cm^2). At first glance, it is apparent that the higher J_{HA} the shorter t_{TC} is, with t_{TC} ~93.5, 51.0 and 25.5 s (i.e. 11, 6 and 3 pulses) for J_{HA} = 290, 325 and 390 mA/cm^2. From this result, it is inferred that higher HA current densities are more favorable for the generation of AANTs since the critical temperature is reached at shorter t_{TC}. Analysis of the output voltage pulses characterizing this process reveal that the rise of voltage amplitude during Section I is much more pronounced as J_{HA} is increased. The increment of V_{amp} during Section I for pulse-anodized AA templates produced with J_{HA} = 290, 325 and 390 mA/cm^2 was 0.935 ± 0.001, 2.785 ± 0.611 and 12.051 ± 0.157 V/pulse, respectively. However, V_{amp} is stabilized after the critical temperature is reached, as indicated by the small variation of this parameter with the number of pulses during Section II. The increment of V_{amp} during Section II was 0.208 ± 0.030, −0.036 ± 0.009 and −0.085 ± 0.007 V/pulse for J_{HA} = 290, 325 and 390 mA/cm^2, respectively. These results indicate that V_{amp} increases slightly with the number of pulses at J_{HA} = 290 mA/cm^2, and remains almost constant at J_{HA} = 325 and 390 mA/cm^2 (i.e. negative but almost negligible change in V_{amp}). Analysis of V_{offset} (Figure S2 – Supplementary data) reveals that this electrochemical parameter follows qualitatively comparable trend to that shown by V_{amp}, with marked increment prior to t_{TC} and stabilizing after reaching the critical temperature at the nanopore's bottom. The increment of V_{offset} within Section I for PA AA templates produced with J_{HA} = 290, 325 and 390 mA/cm^2 was 1.092 ± 0.143, 4.195 ± 1.111 and 0.913 ± 0.370 V/pulse, with maximum and minimum V_{offset} values of 21–33, 20–44 and 22–26 V, respectively. The increment of V_{offset} during Section II is less marked, with rates of 0.268 ± 0.032, 0.017 ± 0.010 and 0.099 ± 0.006 V/pulse for PA AA templates produced with J_{HA} = 290, 325 and 390 mA/cm^2, respectively. The maximum and minimum V_{offset} values within this stage of the anodization process were 37–48, 41–42 and 37–41 V, respectively.

TEM images of free-standing AANTs generated from modulated AA templates produced with J_{HA} = 290, 325 and 390 mA/cm^2 after selective chemical etching and sonication reveal that AANTs increase their length (L_{AANT}) with J_{HA} (Fig. 4a–c). Graphs shown in Fig. 5a and b illustrate the dependence of AANTs' geometric features (L_{AANT}, d_{in} and d_{out}) with J_{HA} for J_{HA} = 290, 325 and 390 mA/cm^2. Fig. 5a reveals a linear correlation between L_{AANT} and J_{HA}, with the former structural feature increasing at a rate of 2.9 ± 0.5 nm/(mA/cm^2) with the latter anodization parameter. AANTs produced with J_{HA} = 290, 325 and 390 mA/cm^2 feature an average total length of 720 ± 96, 847 ± 79 and 1008 ± 118 nm, respectively (distribution histograms shown in Figure S3 – Supplementary data). We also estimated thickness to charge density ratio (x) during hard anodization pulses. For J_{HA} = 290, 325 and 390

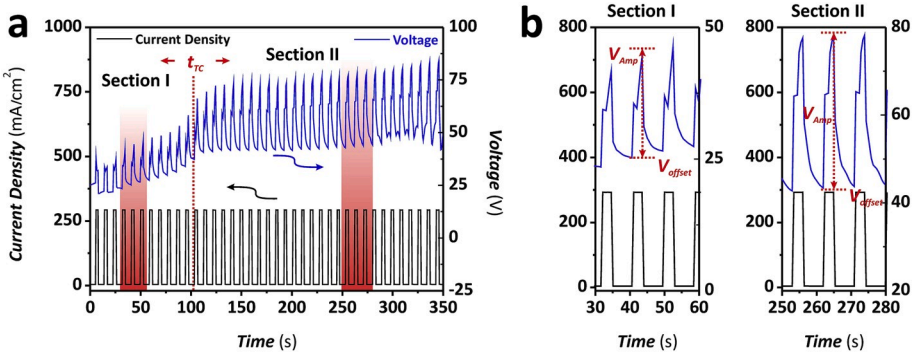

Fig. 3. Analysis of PA profile obtained during the fabrication of AANTs under current density-control conditions (NB: representative profile for HA current density – J_{HA} = 290 mA/cm^2, MA current density – J_{MA} = 4.5 mA/cm^2, time at J_{HA} – t_{HA} = 3.5 s, and time at J_{MA} – t_{MA} = 5 s). (a) PA profile showing the initial increment in voltage amplitude (V_{amp}) and offset (V_{offset}) (Section I) and stabilization of the PA process after reaching the critical temperature at t_{TC} (Section II). (b) Magnified view of current density and voltage pulses (red rectangles in (a)) in the PA profile before (Section I) and after (Section II) reaching the critical temperature at t_{TC}. (For interpretation of the references to color in this figure legend, the reader is referred to the Web version of this article.)

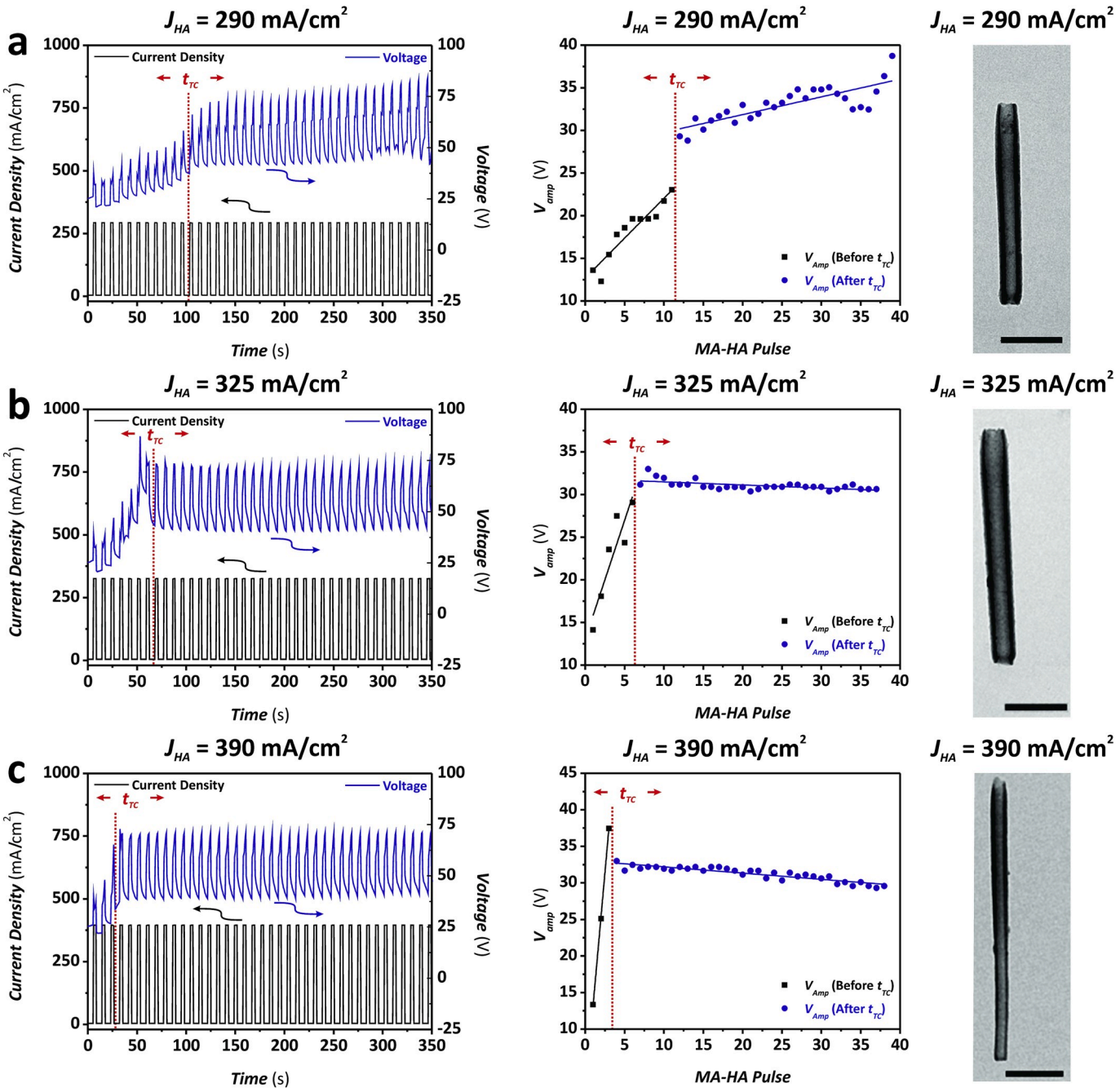

Fig. 4. Analysis of PA profile (voltage amplitude – V_{amp} and offset – V_{offset}) obtained during the fabrication of AANTs under current density-control conditions at different HA current density inputs (J_{HA} = 290, 325 and 390 mA/cm^2) (NB: representative profiles for MA current density – J_{MA} = 4.5 mA/cm^2, time at J_{HA} – t_{HA} = 3.5 s, and time at J_{MA} – t_{MA} = 5 s). (a) Full PA current density/voltage profile showing the initial increment in V_{amp} and V_{offset} and stabilization of the PA process after reaching the critical temperature at t_{TC} (dotted red line) for J_{HA} = 290 mA/cm^2 (left), dependence of V_{amp} with the number of MA-HA pulses before and after reaching the critical temperature at t_{TC} (center), and TEM image of a representative AANT (scale bar: 200 nm). (b) Full PA current density/voltage profile showing the initial increment in V_{amp} and V_{offset} and stabilization of the PA process after reaching the critical temperature at t_{TC} (dotted red line) for J_{HA} = 325 mA/cm^2 (left), dependence of V_{amp} with the number of MA-HA pulses before and after reaching the critical temperature at t_{TC} (center), and TEM image of a representative AANT (scale bar: 200 nm). (c) Full PA current density/voltage profile showing the initial increment in V_{amp} and V_{offset} and stabilization of the PA process after reaching the critical temperature at t_{TC} (dotted red line) for J_{HA} = 390 mA/cm^2 (left), dependence of V_{amp} with the number of MA-HA pulses before and after reaching the critical temperature at t_{TC} (center), and TEM image of a representative AANT (scale bar: 200 nm). (For interpretation of the references to color in this figure legend, the reader is referred to the Web version of this article.)

mA/cm^2, charge value is 83, 93 and 111 mA/cm·s. In all cases, ratio value remains on similar level of 1.40 C/μm·cm^2, which is lower than for typical values for mild anodization sulfuric acid at 25 V (1.70–1.90 C/μm·cm^2) [37]. Analysis of the interplay between J_{HA} and d_{out} and d_{in} is shown in Fig. 5b, revealing a linear dependence between these geometric features and the HA current density input. AANTs produced with J_{HA} = 290, 325 and 390 mA/cm^2 feature an average d_{out} of 98.2 ± 11.4, 81.3 ± 12 and 65.5 ± 10.1 nm, respectively, with a decreasing linear rate of −0.32 ± 0.05 nm/(mA/cm^2). The inner diameter of AANTs fabricated with J_{HA} = 290, 325 and 390 mA/cm^2 has value of 47.9 ± 7.4, 42.1 ± 4.9 and 36.8 ± 5.7 nm, respectively and d_{in} was found to decrease at a linear rate of −0.11 ± 0.02 nm/(mA/cm^2) with J_{HA} under the

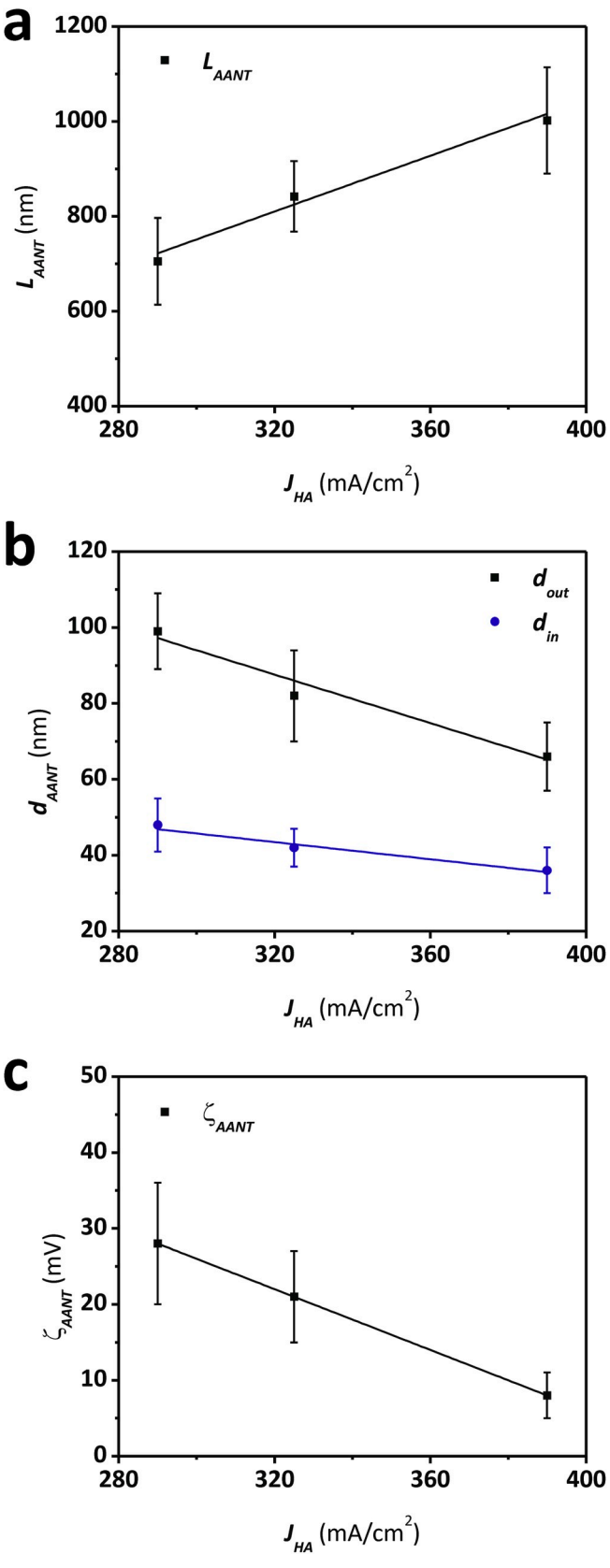

(caption on next column)

Fig. 5. Analysis of effect of HA current density (J_{HA}) on the geometric and physico-chemical properties of AANTs produced by PA. (a) Linear dependence between the total length of AANTs (L_{AANT}) and J_{HA}, in which the later structural feature increases at a rate of 2.9 ± 0.5 nm/(mA/cm^2) with the former anodization parameter. (b) Linear dependence between the outer and inner diameter of AANTs (d_{out} and d_{in}) and J_{HA}, in which the later geometric features decrease at rates of −0.32 ± 0.05 and −0.11 ± 0.02 nm/(mA/cm^2) with the former anodization parameter, respectively. (c) Linear dependence between the ζ-potential of AANTs (ζ_{AANT}) and J_{HA}, in which the later physico-chemical property decreases at a rate of −0.20 ± 0.01 mV/(mA/cm^2) with the former anodization parameter.

conditions of study. To the best of our knowledge, there is no study assessing the impact of the hard anodization current density on the nanotubes' inner and outer diameter. Similar trend, however, has been observed for anodic alumina produced during continuous hard anodization [13,38]. These studies found that the cell size decreases with the current density input. One of the hypothesis regarding creation of these weaker spots is that high current density may result in the formation of less dense forms of alumina, which will also contribute to the nanotube diameter contraction due to partial dissolution of more susceptible alumina upon the acid etching treatment applied during liberation [39]. Control over the geometric features of AANTs is critical to engineer the properties of these 1D nanostructures for specific applications. However, AANTs' physico-chemical properties are also a key factor in determining the applicability of this model nanomaterial in disciplines such as drug delivery and nanotoxicity. Motivated by these results, we analyzed the effect of J_{HA} on the ζ-potential of AANTs produced by pulse anodization.

Fig. 5c indicates that the ζ-potential of AANTs decreases linearly with J_{HA} at a rate of −0.20 ± 0.01 mV/(mA/cm^2) with J_{HA}, where AANTs fabricated with J_{HA} = 290, 325 and 390 mA/cm^2 have a ζ_{AANT} = 25.1 ± 6.8, 19.3 ± 4.7 and 8.6 ± 2.3 mV, respectively. Chemistry of AANTs walls is twofold. While outer surface is rich in hydroxyl group, inside walls contain incorporated sulfate anions [23,40]. During the anodization process, ions from the acid electrolyte are incorporated into the structure of the growing alumina, which features an onion-like distribution of incorporated anions that is higher at the inner layers of the nanopores (i.e. alumina exposed to acid electrolyte) [41]. While in this study we do not evaluate effects of ion incorporation density on resulting zeta potential, it was previously pointed out that sulfate ions are expected to impact behavior of the particles as compared to commercially available alumina nanoparticles [36].

3.4. Effect of hard anodization pulse duration on the physical and chemical properties of AANTs

The duration of the hard anodization pulse (t_{HA}) is another key anodization parameter in controlling the structural and physico-chemical properties of AANTs produced by pulse anodization [30]. However, to the best of our knowledge, no study has performed an in-depth analysis on the impact of this anodization parameter over the physio-chemical properties of AANTs. To assess the impact of this parameter on the geometric features of AANTs, AA templates with a MA starting layer of 100 μm thickness were pulse-anodized at varying hard anodization pulse duration (t_{HA} = 2.0, 2.5 and 3.5 s). The rest of anodization parameters (i.e. MA current density – J_{MA}, HA current density – J_{HA}, and time at J_{MA} – t_{MA}) were kept constant at 4.5 mA/cm^2, 325 mA/cm^2 and 5 s, respectively. Fig. 6a–c shows representative current density–voltage PA anodization profiles at varying HA duration (i.e. t_{HA} = 2.0, 2.5 and 3.5 s). From these graphs, it is apparent that the longer t_{HA} the shorter t_{TC} is, with t_{TC} = 235, 98.5 and 43.5 s (i.e. 33, 14 and 6 pulses) for t_{HA} = 2.0, 2.5 and 3.5 s. This analysis reveals that longer HA durations enable a more optimal generation of AANTs since the critical temperature is reached at shorter t_{TC}. Analysis of the output voltage pulses characterizing this process reveal that the rise of V_{amp} during Section I is more marked as t_{HA} is increased. The increment of V_{amp}

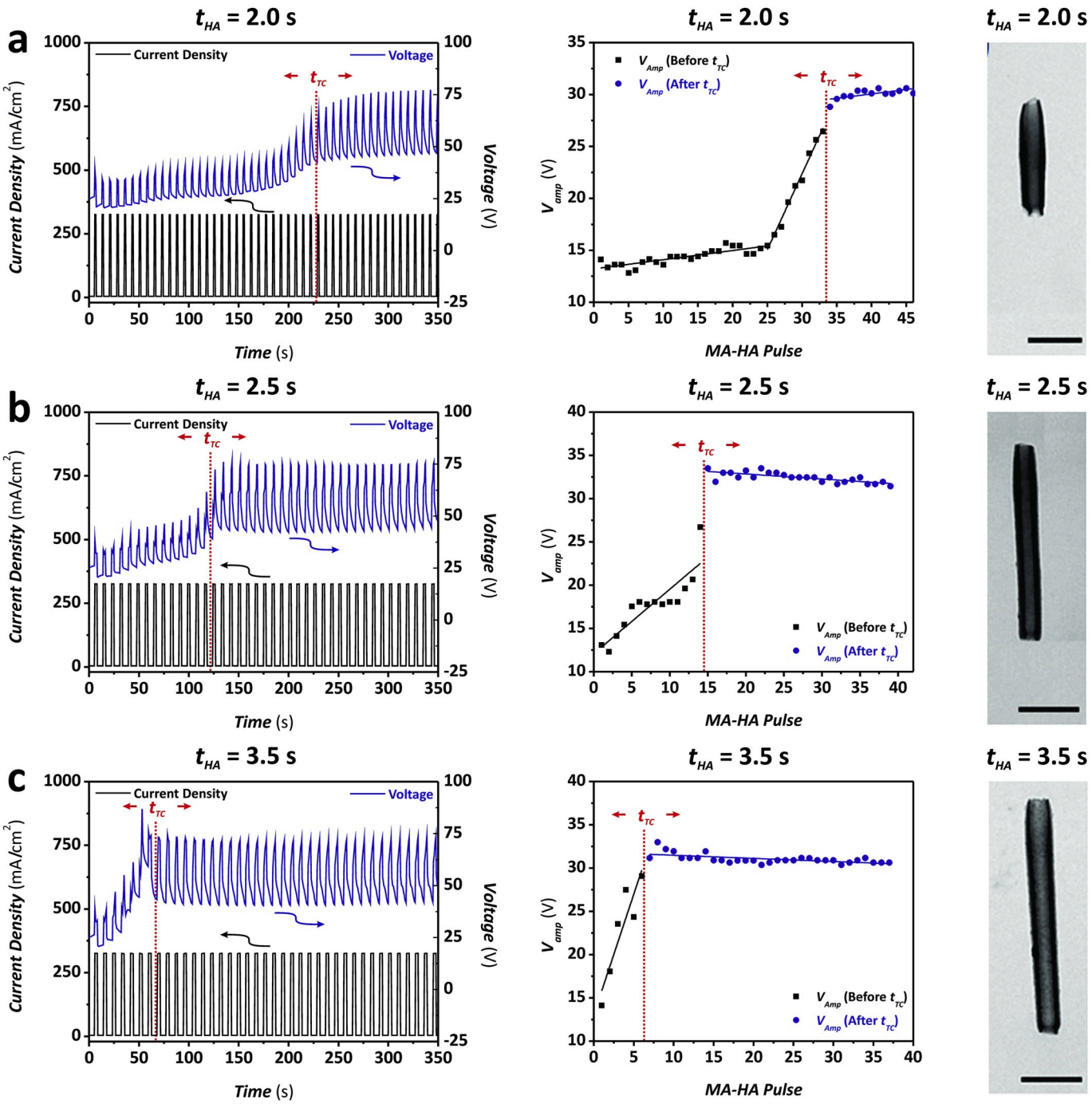

Fig. 6. Analysis of PA profile (voltage amplitude – V_{amp} and offset – V_{offset}) obtained during the fabrication of AANTs under current density-control conditions at different HA durations (t_{HA} = 2.0, 2.5 and 3.5 s) (NB: representative profiles for MA current density – J_{MA} = 4.5 mA/cm^2, HA current density – J_{MA} = 325 mA/cm^2, and time at J_{MA} – t_{MA} = 5 s). (a) Full PA current density/voltage profile showing the initial increment in V_{amp} and V_{offset} and stabilization of the PA process after reaching the critical temperature at t_{TC} (dotted red line) for t_{HA} = 2.0 s (left), dependence of V_{amp} with the number of MA-HA pulses before and after reaching the critical temperature at t_{TC} (center), and TEM image of a representative AANT (scale bar: 200 nm). (b) Full PA current density/voltage profile showing the initial increment in V_{amp} and V_{offset} and stabilization of the PA process after reaching the critical temperature at t_{TC} (dotted red line) for t_{HA} = 2.5 s (left), dependence of V_{amp} with the number of MA-HA pulses before and after reaching the critical temperature at t_{TC} (center), and TEM image of a representative AANT (scale bar: 200 nm). (c) Full PA current density/voltage profile showing the initial increment in V_{amp} and V_{offset} and stabilization of the PA process after reaching the critical temperature at t_{TC} (dotted red line) for t_{HA} = 3.5 s (left), dependence of V_{amp} with the number of MA-HA pulses before and after reaching the critical temperature at t_{TC} (center), and TEM image of a representative AANT (scale bar: 200 nm). (For interpretation of the references to color in this figure legend, the reader is referred to the Web version of this article.)

during Section I for pulse-anodized AA templates produced with t_{HA} = 2.0, 2.5 and 3.5 s was 0.089 ± 0.001, and 0.745 ± 0.115 and 2.785 ± 0.611 V/pulse, respectively. However, it is worthwhile nothing that a 1.462 ± 0.063 V/pulse sharp increment in V_{amp} is observed at t_{HA} = 2.0 s after ~25 pulses (50 s).

Once the critical temperature is reached, V_{amp} stabilizes and the generation of AANTs becomes efficient. This stage is denoted by small variation of this parameter with the number of pulses during Section II.

The increment of V_{amp} during Section II for $t_{HA} = 2.0$, 2.5 and 3.5 s was 0.085 ± 0.027, −0.058 ± 0.011 and −0.036 ± 0.009 V/pulse, respectively. These results reveal that V_{amp} increases slightly with the number of pulses at $t_{HA} = 2.0$ s, and decreases slightly at $t_{HA} = 2.5$ and 3.5. V_{offset} (Figure S4 – Supplementary data) follows a qualitatively comparable trend to that observed for V_{amp}, with marked increment prior to t_{TC} and stabilizing after reaching the critical temperature at the nanopore's bottom. The increment of V_{offset} within Section I for PA AA templates produced with $t_{HA} = 2.0$, 2.5 and 3.5 s was 0.622 ± 0.053, 0.857 ± 0.101 and 4.195 ± 1.111 V/pulse, with maximum and minimum V_{offset} values of 25–35, 25–44 and 25–27 V, respectively. The increment of V_{offset} during Section II is less marked and decreases with increasing t_{HA}, with rates of 0.215 ± 0.019, 0.085 ± 0.019 and 0.017 ± 0.010 V/pulse for PA AA templates produced with $t_{HA} = 2.0$, 2.5 and 3.5 s, respectively. The maximum and minimum V_{offset} values within this stage of the anodization process were 37–49, 41–42 and 37–41 V, respectively. Fig. 6a–c shows TEM images of free-standing AANTs fabricated with $t_{HA} = 2.0$, 2.5 and 3.5 s after selective chemical etching and sonication. At first glance, it is evident that the longer t_{HA} the longer AANTs are. The dependence of AANTs' geometric features (L_{AANT}, d_{in} and d_{out}) with t_{HA} for $t_{HA} = 2.0$, 2.5 and 3.5 s is shown in Fig. 7a and b. Fig. 7a reveals a linear correlation between L_{AANT} and t_{HA}, in which the former structural feature increases at a rate of 268 ± 3 nm/s with the latter anodization parameter. AANTs produced with $t_{HA} = 2.0$, 2.5 and 3.5 s feature an average total length of 424 ± 46, 562 ± 47 and 830 ± 53 nm, respectively (distribution histograms shown in Figure S5 – Supplementary data). Fig. 7b shows analysis of the relationship between t_{HA} and d_{out} and d_{in}. This graph indicates that t_{HA} has small impact on the dimensions of these geometric features in AANTs from 2.0 to 3.5 s. For instance, while d_{out} undergoes a slight linear increment with t_{HA} (i.e. 0.562 ± 0.056 nm/s), d_{in} decreases at a rate of −0.451 ± 0.440 nm/s from $t_{HA} = 2.0$–3.5 s. AANTs produced with $t_{HA} = 2.0$, 2.5 and 3.5 nm/s feature an average d_{out} of 80.1 ± 5.2, 82.8 ± 8.0 and 81.3 ± 6.0 nm, and an average d_{in} of 42.7 ± 4.7, 42.1 ± 3.8 and 42.2 ± 2.4 nm, respectively. Assessment of the effect of the hard anodization duration on the nanotubes' geometric features indicates that, in contrast to J_{HA}, t_{HA} is a suitable anodization parameter to produce AANTs with tunable total length and controlled inner and outer diameter. In other words, t_{HA} makes it possible to fabricate AANTs with distinct length and same inner and outer diameter.

Therefore, t_{HA} provides excellent accuracy to tailor-engineer the length of AANTs without modifying the inner and outer diameter of AANTs. The duration of the hard anodization pulse was also found to moderately impact ζ-potential of AANTs. Fig. 7c shows that ζ_{AANT} increases at a rate of 1.98 ± 0.71 mV/s with t_{HA} from 2.0 to 3.5 s. It is worthwhile noting that the total surface area is higher for shorter nanotubes. So, the influence of the AANTs' inner surface on the average ζ-potential it is expected to be higher in shorter nanotubes. Another factor affecting ζ_{AANT} is the heterogeneous distribution of electrolyte anions following an onion-like structure between the outer and inner layers of AANTs, which also affects the average ζ-potential of these nanostructures.

3.5. Post-treatment modification of AANTs produced by pulse anodization

Pulse anodization provides an effective approach to tune the geometric and physico-chemical features of AANTs. This nanofabrication approach was devised as a cost-effective means for mass-production of AANTs. However, liberation of AANTs from the original pulsed AA template remains challenging, requiring precise-tuning of the post-treatment conditions so nanotubes can be efficiently liberated [42]. This aspect is of paramount importance if we are to enable AANT technology for applications requiring high production yields, such as catalysis and drug delivery. Motivated by this challenge, we studied the effect of different post-treatment processes to selectively weaken the structure of pulsed AA templates and facilitate the liberation of AANTs, including sonication, thermal treatment, and chemical etching.

3.5.1. Effect of sonication parameters on dispersity and separation of AANTs

3.5.1.1. Sonication time. Fabrication of AANTs by pulse anodization is a top-down process in which the anodic alumina structure is typically grinded down by sonication. Weaker spots and crevices along the pulsed AA structure promote the selective breaking of the structure at designed spots, leading to the liberation of nanotubes with controlled geometric features. However, imperfections in the structure of the AA template result in incomplete or partial fragmentation and liberation of nanotubes, minimizing the production yield. A sonication treatment of 1 h performed at room temperature conditions leads to presence of AANTs aggregates and bundles. Fig. 8a shows a schematic showing the impact of the sonication time on AANTs. TEM images of AANTs shown in Fig. 8b reveal a significant change in surface morphology when the sonication time is increased from 1 to 2 h. The surface of AANTs after sonication time >1 h is covered with dust-like nanoparticles, which are thought to be generated from the alumina matrix during the sonication process. Alumina nanoparticles are electrostatically attached onto the surface of AANTs.

Analysis of AANTs' size distribution by DLS shows two distinct peaks associated with the separated fraction and aggregates of AANTs upon 1 and 2 h of sonication treatment (Fig. 8c). After 1 h of sonication treatment, the DLS profile shows a relatively more intense size peak located at ~1400 nm, which corresponds to liberated AANTs. The peak associated with the fraction of unseparated structures is also relatively intense, with an average diameter of ~6 μm. This result indicates that the liberation of nanotubes from the anodic alumina structure is not so effective after 1 h of sonication treatment. However, upon longer sonication time the peak representing the fraction of liberated nanotubes becomes narrower and shifted towards smaller sizes (~820 nm average), indicating that the liberation of nanotubes is much more efficient under such conditions. Furthermore, the size peak from aggregates is significantly reduced. These results indicate that, although longer sonication treatment enhances the liberation of AANTs and minimizes the aggregate fraction, this treatment leads to a partial degradation of the nanotubes' structure.

3.5.1.2. Sonication temperature. The impact of the temperature of the sonication bath on the dispersion and morphology of nanotubes was investigated by performing sonication of nanotubes for 1 h at three different temperatures: 15, 30 and 65 °C. Note that the temperature below ambient conditions was maintained using ice to cool down the sonication bath under constant temperature monitoring. Fig. 9a shows a schematic description of morphological changes in AANTs liberated at different sonication temperatures. From these results it is apparent that increased sonication temperature affects the morphology of AANTs. No visible changes in morphology are observed in nanotubes liberated under sonication at 15 °C (Fig. 9b). Although the structure of AANTs keeps its original morphology, sonication at 30 °C results in formation of a coating layer. When the sonication bath temperature is increased to 65 °C, the degradation of the structure of nanotubes is apparent, with the formation of partially dissolved and unzipped nanotubes forming aggregates without defined shape. DLS size distribution analysis shown in Fig. 9c reveals two major size peaks corresponding to liberated nanotubes and aggregates. While the location of these size peaks remains within similar ranges (~1000 nm for liberated AANTs and ~6 μm for aggregates), their intensity ratio (or relative intensities) varies significantly with the sonication temperature. An increase in sonication temperature leads to the gradual increment and decrement of the size peak associated with the aggregates and liberated nanotubes, respectively.

Several factors are thought to promote the formation of nanotubes aggregates under these conditions. Different sonication bath

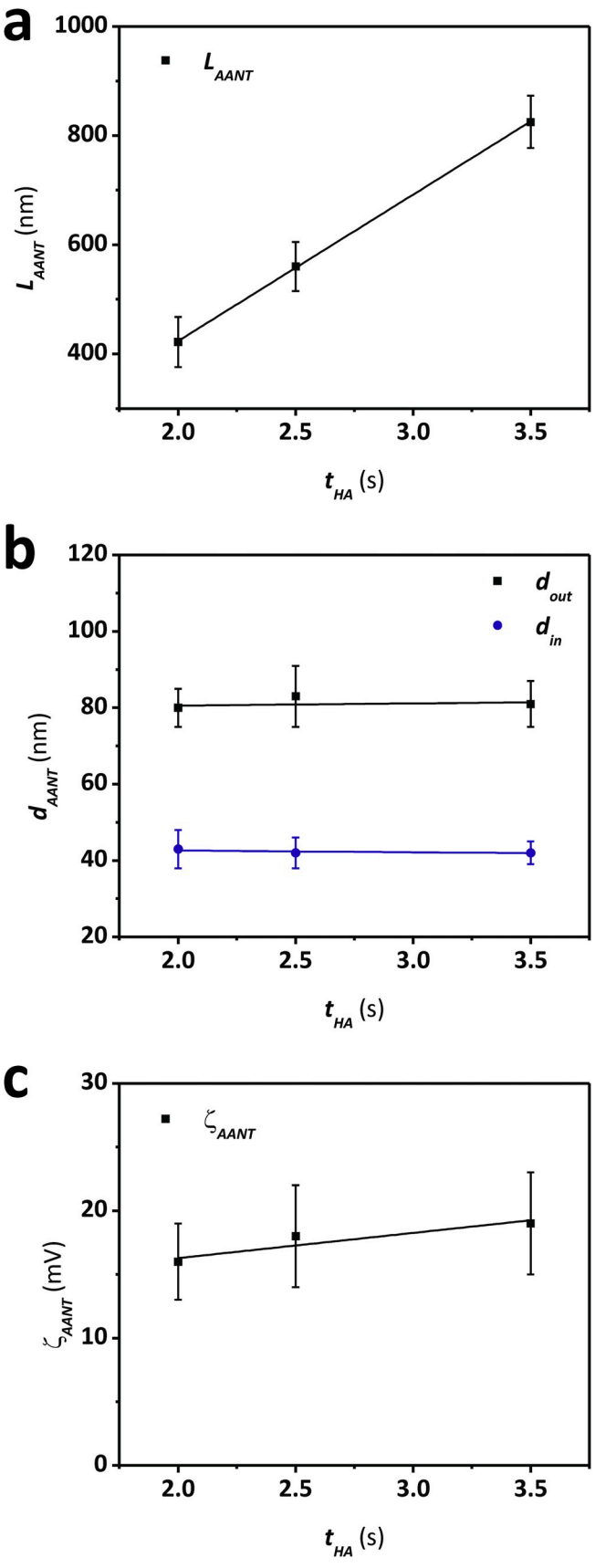

(caption on next column)

Fig. 7. Analysis of effect of HA duration (t_{HA}) on the geometric and physico-chemical properties of AANTs produced by pulse anodization. (a) Linear dependence between the total length of AANTs (L_{AANT}) and t_{HA}, in which the later structural feature increases at a rate of 268 ± 3 nm/s with the former anodization parameter. (b) Linear dependence between the outer and inner diameter of AANTs (d_{out} and d_{in}) and t_{HA}, in which the later geometric features vary at rates of 0.562 ± 0.056 and −0.451 ± 0.440 nm/s with the former anodization parameter, respectively. (c) Linear dependence between the ζ-potential of AANTs (ζ_{AANT}) and t_{HA}, in which the later physico-chemical property increases at a rate of 1.98 ± 0.71 mV/s with the former anodization parameter.

temperature results in increasing number of nanotube–nanotube interactions. Brownian motion of AANTs is faster at higher temperature, resulting in more frequent interactions between nanotubes, which may weaken the mechanical strength of AANTs. Also, viscosity of water at 65 °C is 2.7 times lower than of water at 15 °C. Higher viscosity can increase shear forces between individual nanotubes, promoting a more efficient separation. Other factors such as cavitation could also have an impact on the AANTs' structure at different sonication temperatures [43,44]. Additionally, a combination of temperature and sonication could promote the formation of hydrated forms of alumina, which in turn would weaken the structure of AANTs [45]. To summarize, sonication at lower temperature provides the best separation yield within the conditions of study, preventing AANTs from undesired degradation.

3.5.2. Effect of annealing temperature on the crystallinity and physio-chemical properties of AANTs

Aluminum oxide (Al_2O_3) can feature amorphous and several crystalline phases. The composition of the crystalline phase of anodic alumina depends on the fabrication process and its processing conditions. Phase transition of initially amorphous AA can be induced with annealing. Formation of crystallites occurs with annealing above 700 °C when gamma alumina emerge. Then, at temperature above 1100 °C another crystalline form, alpha alumina appear initially as a small fraction. Further increasing temperature, ratio of gamma to alpha crystalline forms decrease and above 1200 °C only alpha alumina form can be detected. Alpha alumina exhibit far higher resistance to acid and chemical etching, compared to other crystalline and amorphous forms [46]. Thermal and chemical resistance along with other physical properties makes anodic alumina attractive material platform amongst other ceramic-base materials [47]. In order to analyze impact of the annealing temperature on the phase composition of AANTs, a set of pulsed AA structures were exposed to thermal treatment at different temperatures: 850, 1050 and 1200 °C. Annealed pulsed AA templates and liberated AANTs were analyzed by XRD, TEM, DLS, SEM (Fig. 10). As-produced AANTs have a smooth surface. However, small morphological changes can already be observed in AANTs after annealing at 850 °C. These AANTs show small pits homogeneously distributed across their surface and much darker walls, denoting a much dense form of alumina upon 850 °C thermal treatment (Fig. 10a). These changes might be associated with decomposition of electrolyte anions and water loss from the Al_2O_3 structure, and starting transition of its crystallographic phase into gamma Al_2O_3. EDS analysis (Figure S6 – Supplementary data) reveals that the elemental concentration of sulfur in AANTs decreases by a 77% (from 12.2% to 2.8%) upon thermal annealing at 850 °C. This analysis also indicates a slight decrement in oxygen content – from 45.22% to 41.9% – and a noticeable increment in the relative content of aluminum from 42.6% to 55.3%. As annealing temperature increases, morphological changes in AANTs become more apparent. AANTs show higher granulation on their surface after thermal annealing at 1050 °C. This may be associated with further removal of sulfur from their structure, the content of which decreases to 0.82% due to oxidation and gradual release of SO_2 gas. Gas release might induce morphological changes in the structure of AANTs [48]. Deformation of the AANTs' walls also becomes substantial under these conditions. Much apparent morphological changes can be observed in nanotubes annealed at 1200 °C. While

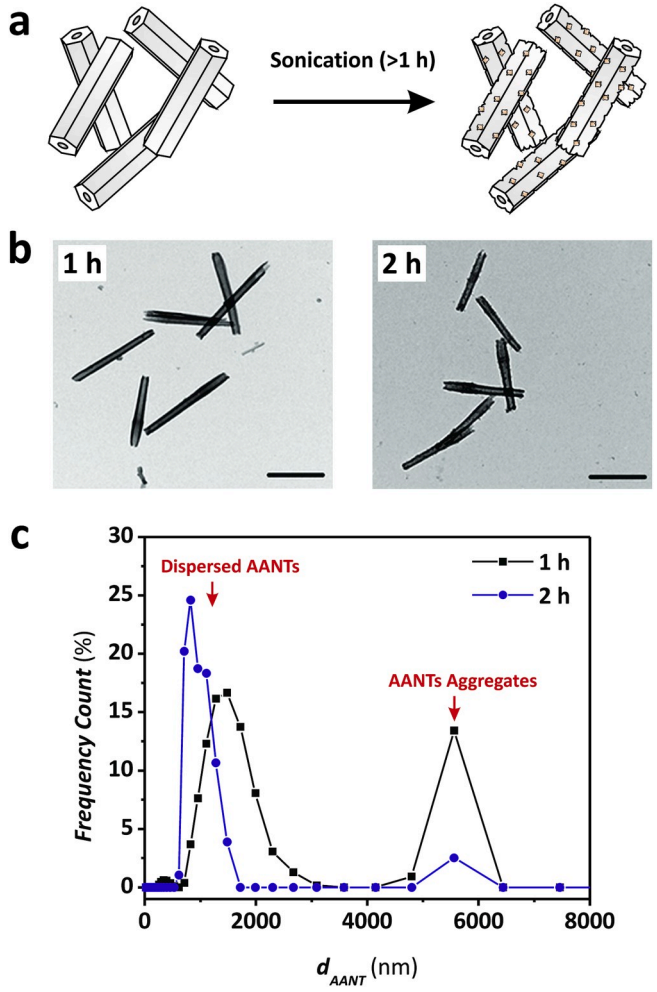

Fig. 8. Effect of sonication time on the dispersity and morphology of AANTs fabricated by pulse anodization (NB: AANTs fabricated with $J_{MA} = 4.5$ mA/cm^2, $J_{MA} = 325$ mA/cm^2, $t_{MA} = 5$ s and $t_{HA} = 3.5$ s). (a) Schematic illustrating the impact of sonication (1 and 2 h) on the morphology of AANTs. (b) TEM images of AANTs after 1 h (left) and 2 h (right) of sonication (scale bars: 500 nm). (c) DLS size distribution of AANTs after 1 and 2 h of sonication.

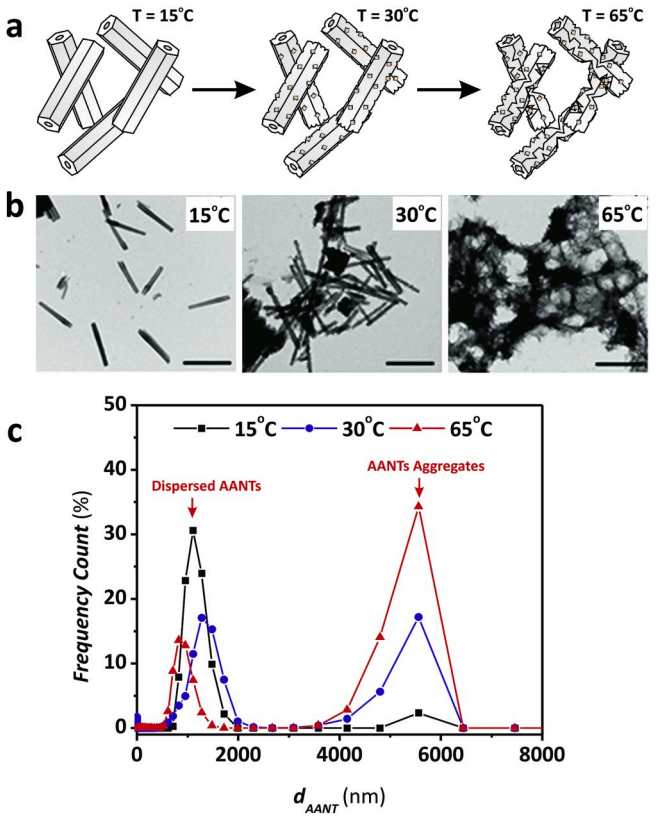

Fig. 9. Effect of bath temperature on the dispersity and morphology of AANTs fabricated by pulse anodization (NB: AANTs fabricated with $J_{MA} = 4.5$ mA/cm^2, $J_{MA} = 325$ mA/cm^2, $t_{MA} = 5$ s and $t_{HA} = 3.5$ s). (a) Schematic illustrating the impact of the bath temperature (15, 30 and 65 °C) on the morphology of AANTs. (b) TEM images of AANTs at 15 °C (left), 30 °C (center) and 65 °C (right) bath temperature (scale bars: 1 μm). (c) DLS size distribution of AANTs after liberation in 15, 30 and 65 °C bath temperature.

nanotubes still exhibit elongated shape, the initial nanotubular structure is completely lost. No walls or hollow space inside the nanotubes can be observed, suggesting complete collapse of the structure and the formation of fiber-like aluminum oxide nanoparticles. Additionally, EDX analysis indicates that sulfur has been completely removed from the AANTs' structure. XRD analysis of AANTs reveal no crystalline phases for as-produced AANTs. Subtle changes in diffractogram patterns can be observed at 850 °C (Fig. 10b) with presence of peaks at 39.43° (2 2 2), 45.85° (4 0 0) and 66.85° (4 4 0) that are attributed to gamma Al_2O_3. Presence of crystalline phase is more pronounced with sample annealed at 1050 °C, with gamma Al_2O_3 alumina phase denoted by major reflection peaks at 39.43° (2 2 2), 45.85° (4 0 0) and 66.85° (4 4 0) and slightly visible peaks at 32.85° (2 2 0), 36.85° (3 1 1) and 61.25° (5 1 1) in the XRD diffractogram (JCPDS cards nos. 00-056-0457). Crystallographic phase transition can induce morphological alterations in the structure of AANTs. As the annealing temperature is raised to 1200 °C, a considerable change in the XRD spectrum is observed. Peaks of gamma Al_2O_3 are not visible anymore, instead, sharp peaks of alpha-Al_2O_3 can be observed. Peaks are present at 25.60° (0 1 2), 35.15° (1 0 4), 37.80° (1 1 0), 43.36° (1 1 3), 52.55° (0 2 4), 57.50° (1 1 6), 66.50° (2 1 4) and 68.25° (3 0 0) (JCPDS cards nos. 00-046-1212) and represent only alpha-Al_2O_3. The annealing temperature is also found to impact the surface charge of liberated AANTs. Fig. 10c shows the effect of this post-treatment parameter on the ζ-potential of AANTs. Reference non-annealed AANTs have a ζ-potential of ~19 mV. As the annealing temperature increases, ζ_{AANT} decreases to 10 and 5 mV at annealing temperatures of 850 and 1050 °C, respectively. This surface charge decrement may be attributed to the decrease in sulfur content and hydroxide groups (i.e. water loss) in the structure of AANTs [48]. Further annealing at 1200 °C makes ζ_{AANT} negative (−7 mV). Under such conditions, sulfur is completely removed from the structure of AANTs, changing the charge of these 1D nanostructures dramatically [48,49].

4. Conclusions

In summary, this is a systematic study on the influence of different anodization conditions and post-fabrication treatments on the physical and chemical properties of anodic alumina nanotubes fabricated by current density–control pulse anodization. Our results indicate that the current density input can be readily used as a fabrication parameter to tailor-engineer the AANTs' features such as the inner and outer diameters, the total length and the surface charge. We have demonstrated that higher current density values during hard anodization pulses promote lower surface charge and more narrow shape of nanotubes. A linear dependence between the hard anodization pulse duration and nanotubes average length demonstrates that the hard anodization pulse duration a precise parameter to tailor the nanotubes' length without changing the inner and outer diameters. A systematic optimization of the pulse anodization process has allowed us to fabricate the shortest nanotubes reported so far, with average length of 422 ± 46 nm. Additionally, different sonication parameters were examined to optimize the

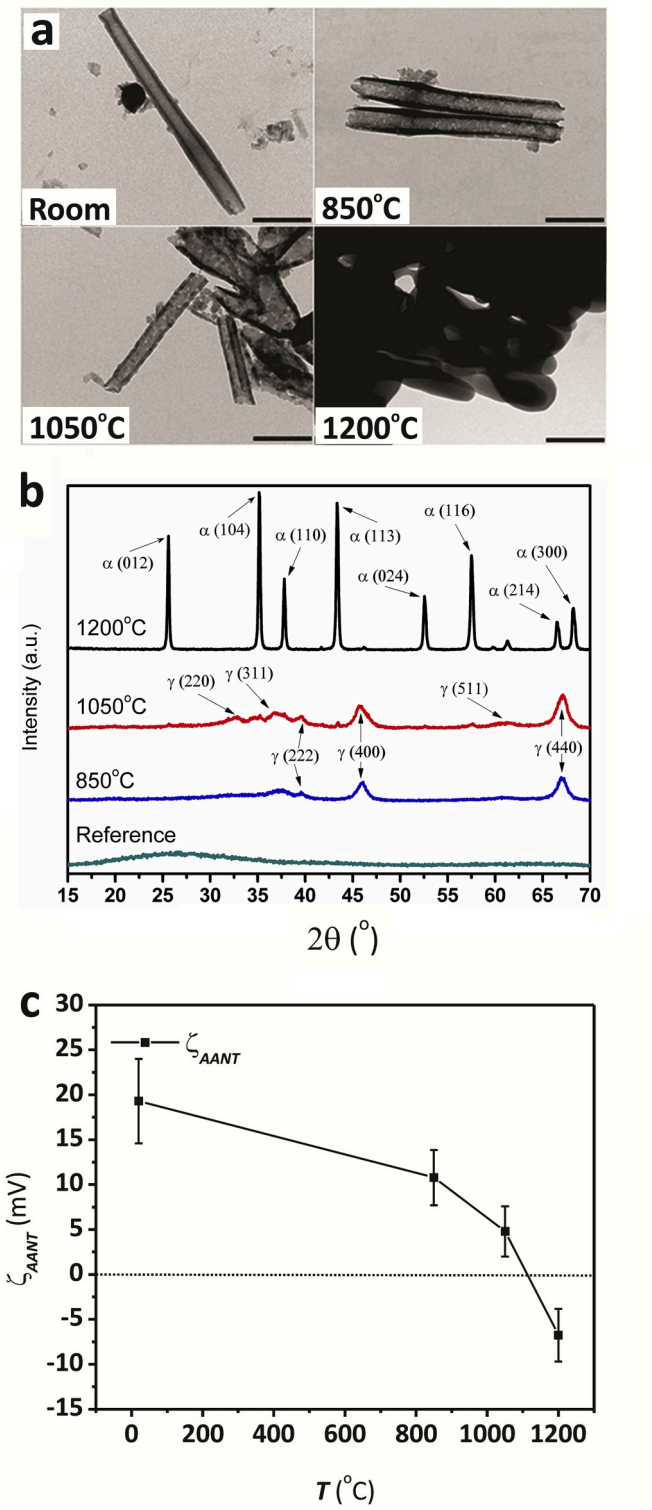

Fig. 10. Effect of annealing temperature on morphology, crystallographic phase and physico-chemical properties of AANTs produced by pulse anodization (NB: AANTs fabricated with $J_{MA} = 4.5$ mA/cm^2, $J_{MA} = 325$ mA/cm^2, $t_{MA} = 5$ s and $t_{HA} = 3.5$ s). (a) TEM images of AANTs at room, 850, 1050 and 1200 °C (scale bars: 200 nm). (b) XRD spectra of AANTs at room, 850, 1050 and 1200 °C. (c) Change in ζ-potential of AANTs (ζ_{AANT}) with annealing temperature (T).

liberation of AANTs. However, the structure of AANTs is found to be compromised at long sonication times (>1 h) and high sonication bath temperatures (>40 °C). The combination of low sonication bath (15 °C) with moderate sonication time (1 h) is found to be the most optimal approach to increase the production yield of AANTs while maintaining the structural integrity of these nanostructures. Our study also demonstrates that a post-fabrication annealing treatment can be used to alter the crystalline phase composition and ζ-potential of nanotubes. However, high annealing temperatures (>850 °C) lead to a gradual structural degradation of AANTs due to decomposition of sulfur and water loss. This study provides new insights to better understand the impact of the fabrication parameters over the physical and chemical properties of AANTs produced by pulse anodization. This step forward in AANTs technology could provide new and exciting opportunities to design and tailor-engineer these model 1D nanostructures for specific applications, including catalysis, drug delivery, nanofabrication and sensing.

Declaration of competing interest

The authors declare that they have no known competing financial interests or personal relationships that could have appeared to influence the work reported in this paper.

CRediT authorship contribution statement

J.T. Domagalski: Writing - original draft, Methodology, Investigation, Writing - review & editing. **E. Xifre-Perez:** Methodology, Validation, Writing - review & editing. **A. Santos:** Conceptualization, Validation, Formal analysis, Writing - review & editing. **J. Ferre-Borrull:** Formal analysis, Data curation. **L.F. Marsal:** Conceptualization, Validation, Resources, Supervision, Project administration, Funding acquisition.

Acknowledgments

This work was supported in part by the Spanish Ministerio de Ciencia, Innovación y Universidades (MICINN)/(FEDER) RTI2018-094040-B-I00, by the Agency for Management of University and Research Grants (AGAUR) 2017-SGR-1527 and by the Catalan Institution for Research and Advanced Studies (ICREA) under the ICREA Academia Award. This project has received funding from the European Union's Horizon 2020 research and innovation program under the Marie Sklodowska-Curie grant agreement No. 713679 and from the Universitat Rovira i Virgili (URV). Authors also thank the support provided by the Australian Research Council through the grant number CE140100003, the School of Chemical Engineering, The University of Adelaide, the Institute for Photonics and Advanced Sensing, the ARC Centre of Excellence for Nanoscale BioPhotonics.

Appendix A. Supplementary data

Supplementary data to this article can be found online at https://doi.org/10.1016/j.micromeso.2020.110264.

References

[1] A.K. Vijh, Sparkling voltages and side reactions during an anodization of valve metals in terms of electron tunneling, Corrosion Sci. 11 (1971) 411.
[2] F. Li, L. Zhang, R.M. Metzger, On the growth of highly ordered pores in anodized aluminum oxide, Chem. Mater. 10 (1998) 2470.
[3] W. Lee, S.J. Park, Porous anodic aluminum oxide: anodization and templated synthesis of functional nanostructures, Chem. Rev. 114 (2014) 7487.
[4] A. Santos, L. Vojkuvka, M. Alba, V.S. Balderrama, J. Ferre-Borrull, J. Pallares, L. F. Marsal, Understanding and morphology control of pore modulations in nanoporous anodic alumina by discontinous anodization, Phys. Status Solidi 209 (2012) 2045.
[5] A. Santos, J. Ferre-Borrull, J. Pallares, L.F. Marsal, Hierarchical nanoporous anodic alumina templates by asymmetric two-step anodization, Phys. Status Solidi 208 (2011) 668.

[6] H. Masuda, Self-ordering of cell arrangement of anodic porous alumina formed in sulfuric acid solution, J. Electrochem. Soc. 144 (1997) L127.
[7] A. Santos, T. Kumeria, D. Losic, Nanoporous anodic aluminum oxide for chemical sensing and biosensors, Trends Anal. Chem. 44 (2013) 25.
[8] C.T. Sousa, D.C. Leitao, M.P. Proenca, J. Ventura, A.M. Pereira, J.P. Araujo, Nanoporous alumina as templates for multifunctional applications, Appl. Phys. Rev. 1 (2014), 031102.
[9] K. Nielsch, J. Choi, K. Schwirn, R.B. Wehrspohn, Self-ordering regimes of poorus alumina: the 10% porosity rule, Nano Lett. 2 (2002) 1.
[10] Y.V. Nazarkina, S.A. Gavrilov, A.A. Polohin, D. Gromov, Y.P. Shaman, Application of porous alumina formed in selenic acid solution for nanostructures investigation via Raman spectroscopy, Int. Conf. Micro- Nano- Electronics 10224 (2016) 102240J.
[11] E.O. Gordeeva, I.V. Roslyakov, K.S. Napolskii, Aluminium anodizing in selenic acid: electrochemical behaviour, porous structure, and ordering regimes, Electrochim. Acta 307 (2019) 13.
[12] S. Akiya, T. Kikuchi, S. Natsui, N. Sakaguchi, R.O. Suzuki, Self-ordered porous alumina fabricated via phosphonic acid anodizing, Electrochim. Acta 190 (2016) 471.
[13] L. Yi, L. Zhiyuan, H. Xing, L. Yisen, C. Yi, Investigation of intrinsic mechanisms of aluminium anodization processes by analyzing the current density, RSC Adv. 2 (2012) 5164.
[14] K. Schwirn, W. Lee, R. Hillebrand, M. Steinhart, K. Nielsch, U. Gösele, Self-ordered anodic aluminum oxide formed by H2SO4 hard anodization, ACS Nano 2 (2008) 302.
[15] L. Zaraska, G.D. Sulka, M. Jaskula, Anodic alumina membranes with defined pore diameters and thicknesses obtained by adjusting the anodizing duration and pore opening/widening time, J. Solid State Electrochem. 15 (2011) 2427.
[16] A. Santos, P. Formentin, J. Pallares, J. Ferre-Borrull, L.F. Marsal, Structural engineering of nanoporous anodic alumina funnels with high aspect ratio, J. Electroanal. Chem. 655 (2011) 73.
[17] P. Csokan, Some observations on the growth mechanism of hard anodic oxide coatings on aluminium, Trans. IMF 41 (1964) 51.
[18] C. Lammel, M. Schneider, C. Heubner, W. Beckert, A. Michaelis, Investigations of burning phenomena during the hard anodising of aluminium by local in-operando temperature measurements, Electrochim. Acta 249 (2017) 271.
[19] W. Lee, R. Ji, U. Gösele, K. Nielsch, Fast fabrication of long-range ordered porous alumina membranes by hard anodization, Nat. Mater. 5 (2006) 741.
[20] I.V. Roslyakov, E.O. Gordeeva, K.S. Napolskii, Role of electrode reaction kinetics in self-ordering of porous anodic alumina, Electrochim. Acta 241 (2017) 362.
[21] V. Vega, J. Garcia, J.M. Montero-Moreno, B. Hernando, J. Bachmann, V.M. Prida, K. Nielsch, Unveiling the hard anodization regime of aluminum: insight into nanopores self-organization and growth mechanism, ACS Appl. Mater. Interfaces 7 (2015) 28682.
[22] Y.C. Ha, D.Y. Jeong, Fast fabrication of a high-aspect-ratio, self-ordered nanoporous alumina membrane by using high-field anodization, J. Kor. Phys. Soc. 57 (2010) 1661.
[23] W. Lee, K. Schwirn, M. Steinhart, E. Pippel, R. Scholz, U. Gösele, Structural engineering of nanoporous anodic aluminium oxide by pulse anodization of aluminium, Nat. Nanotechnol. 3 (2008) 234.
[24] G.D. Sulka, A. Brzozka, L. Liu, Fabrication of diameter-modulated and ultrathin porous nanowires in anodic aluminum oxide templates, Electrochim. Acta 56 (2011) 4972.
[25] Y. Chen, A. Santos, Y. Wang, T. Kumeria, J. Li, Ch Wang, D. Losic, Biomimetic nanoporous anodic alumina distributed bragg reflectors in the form of films and microsized particles for sensing applications, ACS Appl. Mater. Interfaces 7 (2015) 19816.
[26] J. Ferre-Borrull, J. Pallares, G. Macias, L.F. Marsal, Nanostructural engineering of nanoporous anodic alumina for biosensing applications, Materials 7 (2014) 5225.
[27] A. Santos, J.H. Yoo, C.V. Rohatgi, T. Kumeria, Y. Wang, D. Losic, Realisation and advanced engineering of true optical rugate filters based on nanoporous anodic alumina by sinusoidal pulse anodisation, Nanoscale 8 (2016) 1360.
[28] Y. Chen, A. Santos, Y. Wang, T. Kumeria, C. Wang, J. Li, Interferometric nanoporous anodic alumina photonic coatings for optical sensing, Nanoscale 7 (2015) 7770.
[29] Y.F. Mei, X.L. Wu, X.F. Shao, G.G. Siu, X.M. Bao, Formation of an array of isolated alumina nanotubes, Europhys. Lett. 62 (2003) 595.
[30] W. Lee, R. Scholz, U. Gösele, A continuous process for structurally well-defined Al_2O_3 nanotubes based on pulse anodization of aluminum, Nano Lett. 8 (2008) 2155.
[31] Y.F. Mei, X.L. Wu, X.F. Shao, G.S. Huang, G.G. Siu, Formation mechanism of alumina nanotube array, Phys. Lett. Sect. A Gen. At. Solid State Phys. 309 (2003) 109.
[32] S.Z. Chu, K. Wada, S. Inoue, M. Isogai, A. Yasumori, Fabrication of ideally ordered nanoporous alumina films and integrated alumina nanotubule arrays by high-field anodization, Adv. Mater. 17 (2005) 2115.
[33] Y. Wang, A. Santos, A. Evdokiou, D. Losic, Rational design of ultra-short anodic alumina nanotubes by short-time pulse anodization, Electrochim. Acta 154 (2015) 379.
[34] Y. Wang, G. Kaur, Y. Chen, A. Santos, D. Losic, A. Evdokiou, Bioinert anodic alumina nanotubes for targeting of endoplasmic reticulum stress and autophagic signaling: a combinatorial nanotube-based drug delivery system for enhancing cancer therapy, ACS Appl. Mater. Interfaces 7 (2015) 27140.
[35] Y. Wang, G. Kaur, A. Zysk, V. Liapis, S. Hay, A. Santos, D. Losic, A. Evdokiou, Systematic invitro nanotoxicity study on anodic alumina nanotubes with engineered aspect ratio: understanding nanotoxicity by a nanomaterial model, Biomaterials 46 (2015) 117.
[36] Y. Wang, A. Santos, G. Kaur, A. Evdokiou, D. Losic, Structurally engineered anodic alumina nanotubes as nano-carriers for delivery of anticancer therapeutics, Biomaterials 35 (2014) 5517.
[37] I.V. Roslyakov, D.S. Koshkodaev, A.A. Eliseev, D. Hermida-Merino, V.K. Ivanov, A. V. Petukhov, K.S. Napolskii, Growth of porous anodic alumina on low-index surfaces of Al single crystals, J. Phys. Chem. C 121 (2017) 27511.
[38] C. Cheng, A.H.W. Ngan, Fast fabrication of self-ordered anodic porous alumina on oriented aluminum grains by high acid concentration and high temperature anodization, Nanotechnology 24 (2013) 215602.
[39] S. Zhao, K. Chan, A. Yelon, T. Veres, Novel structure of AAO film fabricated by constant current anodization, Adv. Mater. 19 (2007) 3004.
[40] A.A. Tsyganenko, P.P. Mardilovich, Structure of alumina surfaces, J. Chem. Soc. Faraday. Trans. 92 (1996) 4843.
[41] G.C. Wood, A model for the incorporation of electrolyte species into anodic alumina, J. Electrochem. Soc. 143 (2006) 74.
[42] A. Santos, M.J. Deen, L.F. Marsal, Low-cost fabrication technologies for nanostructures: state-of-the-art and potential, Nanotechnology 26 (2015), 042001.
[43] F. Ali, L. Reinert, J.-M. Leveque, L. Duclaux, F. Muller, S. Saeed, S.S. Shah, Effect of sonication conditions: solvent, time, temperature and reactor type on the preparation of micron sized vermiculite particles, Ultrason. Sonochem. 21 (2013) 1002.
[44] L. Dumee, K. Sears, J. Schütz, N. Finn, M. Duke, S. Gray, Influence of the sonication temperature on the debundling kinetics of carbon nanotubes in propan-2-ol, Nanomaterials 3 (2013) 70.
[45] W. Vedder, D.A. Vermilyea, Aluminum + water reaction, Trans. Faraday Soc. 65 (1969) 561.
[46] L.F. Marsal, L. Vojkuvka, P. Formentin, J. Pallares, J. Ferre-Borrull, Fabrication and optical characterization of nanoporous alumina films annealed at different temperatures, Opt. Mater. 31 (2009) 860.
[47] M. Fuji, M.T. Takashi Shirai, Hideo Watanabe, Structural properties and surface characteristics on aluminum oxide powders, Mater. Sci. 9 (2009) 23.
[48] R. Ozao, M. Ochiai, H. Yoshida, Y. Ichimura, T. Inada, Preparation of γ-alumina membranes from sulphuric electrolyte anodic alumina and its transition to α-alumina, J. Therm. Anal. Calorim. 64 (2001) 923.
[49] M.R. Das, J.M. Borah, W. Kunz, B.W. Ninham, S. Mahiuddin, Ion specificity of the zeta potential of α-alumina, and of the adsorption of p-hydroxybenzoate at the α-alumina-water interface, J. Colloid Interface Sci. 344 (2010) 482.